Incommensurate Modulation and Luminescence in the CaGd$_{2(1-x)}$Eu$_{2x}$(MoO$_4$)$_{4(1-y)}$(WO$_4$)$_{4y}$ (0 ≤ x ≤ 1, 0 ≤ y ≤ 1) Red Phosphors

Vladimir A. Morozov,[†,‖] Anne Bertha,[†] Katrien W. Meert,[‡,§] Senne Van Rompaey,[†] Dmitry Batuk,[†] Gerardo T. Martinez,[†] Sandra Van Aert,[†] Philippe F. Smet,[‡,§] Maria V. Raskina,[‖] Dirk Poelman,[‡,§] Artem M. Abakumov,[†] and Joke Hadermann*,[†]

[†]EMAT, University of Antwerp, Groenenborgerlaan 171, Antwerp B-2020, Belgium

[‡]Lumilab, Department of Solid State Sciences, Ghent University, B-9000 Ghent, Belgium

[§]Center for Nano- and Biophotonics (NB-Photonics), Ghent University, B-9000 Ghent, Belgium

[‖]Chemistry Department, Moscow State University, 119991 Moscow, Russia

ⓢ *Supporting Information*

ABSTRACT: Scheelite related compounds $(A',A'')_n[(B',B'')O_4]_m$ with B', B'' = W and/or Mo are promising new light-emitting materials for photonic applications, including phosphor converted LEDs (light-emitting diodes). In this paper, the creation and ordering of A-cation vacancies and the effect of cation substitutions in the scheelite-type framework are investigated as a factor for controlling the scheelite-type structure and luminescent properties. CaGd$_{2(1-x)}$Eu$_{2x}$(MoO$_4$)$_{4(1-y)}$(WO$_4$)$_{4y}$ (0 ≤ x ≤ 1, 0 ≤ y ≤ 1) solid solutions with scheelite-type structure were synthesized by a solid state method, and their structures were investigated using a combination of transmission electron microscopy techniques and powder X-ray diffraction. Within this series all complex molybdenum oxides have (3 + 2)D incommensurately modulated structures with superspace group $I4_1/a(\alpha,\beta,0)00(-\beta,\alpha,0)00$, while the structures of all tungstates are (3 + 1)D incommensurately modulated with superspace group $I2/b(\alpha\beta0)00$. In both cases the modulation arises because of cation-vacancy ordering at the A site. The prominent structural motif is formed by columns of A-site vacancies running along the c-axis. These vacant columns occur in rows of two or three aligned along the $[\bar{1}10]$ direction of the scheelite subcell. The replacement of the smaller Gd^{3+} by the larger Eu^{3+} at the A-sublattice does not affect the nature of the incommensurate modulation, but an increasing replacement of Mo^{6+} by W^{6+} switches the modulation from (3 + 2)D to (3 + 1)D regime. Thus, these solid solutions can be considered as a model system where the incommensurate modulation can be monitored as a function of cation nature while the number of cation vacancies at the A sites remain constant upon the isovalent cation replacement. All compounds' luminescent properties were measured, and the optical properties were related to the structural properties of the materials. CaGd$_{2(1-x)}$Eu$_{2x}$(MoO$_4$)$_{4(1-y)}$(WO$_4$)$_{4y}$ phosphors emit intense red light dominated by the $^5D_0-^7F_2$ transition at 612 nm, along with other transitions from the $^5D_1$ and $^5D_0$ excited states. The intensity of the $^5D_0-^7F_2$ transition reaches a maximum at x = 0.5 for y = 0 and 1.
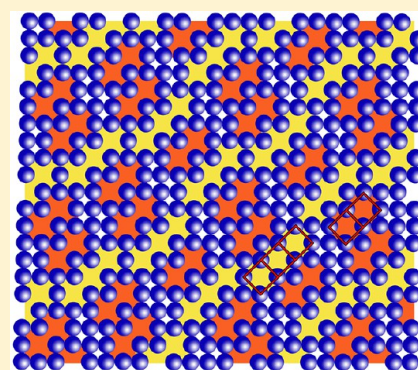
KEYWORDS: *incommensurately modulated structures, transmission electron microscopy, luminescent properties*

1. INTRODUCTION

Trivalent europium (Eu^{3+}) has played a major role in the past decades as a luminescent ion in both display and general lighting applications.[1] Its luminescence originates from internal 4f^6-4f^6 electronic transitions, leading to very narrow emission bands mainly in the orange to red part of the visible spectrum. The local symmetry influences the relative intensity of these emission peaks, allowing a saturated red emission color in hosts with low symmetry.[2] This has led to the use of Eu^{3+}-based phosphors (e.g., Y$_2$O$_2$S:Eu^{3+}) in cathode ray tubes for television and computer displays. Although nowadays attention is shifted away from Eu^{3+} toward Eu^{2+} and Ce^{3+} as dopants because of the tunable emission spectrum,[4−6] Eu^{3+} remains an interesting luminescent ion because of good color saturation, high spectral sensitivity by the human eye, and high luminous efficacy

(LE).[7−9] Therefore, Eu^{3+}-based phosphors can have a future in both display backlighting and light sources with relatively low color rendering, where the excitation flux is not too high.[3,8] Eu^{3+} has an excitation band at 465 nm, due to the $^7F_0-^5D_2$ absorption, which coincides with the emission of blue LEDs. This has led to many recent reports on Eu^{3+} phosphors for use in combination with blue LEDs, including Eu-doped scheelites.[2,10−12]

The scheelite-type ABO_4 (CaWO$_4$) structure is built up by [...-AO_8 - BO_4- ...] columns along the c-axis, as shown in Figure 1. AO_8 polyhedra and BO_4 tetrahedra share common vertices
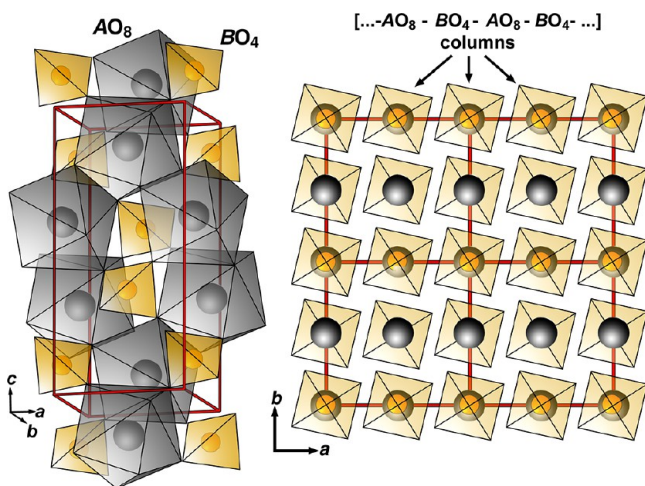
Figure 1. Polyhedral view (left) and *ab* projection of the scheelite-type structure (right). Gray spheres are calcium cations and yellow spheres are tungsten. For clarity, the CaO_8 polyhedra are not shown in the right side image.

and form a 3D framework. A partial substitution is possible of the *A* and/or *B* cations to a composition $(A',A'')_n[(B',B'')O_4]_n$ (*A'*, *A''* = alkali, alkaline-earth or rare-earth elements; *B'*, *B''* = Mo, W) with often good optical properties, good stability, and a relatively simple preparation. For example, $NaEu(WO_4)_2$ and $KGd_{0.75}Eu_{0.25}(MoO_4)_2$ show strong, saturated red emission.[10,11,13] Scheelites can be prepared with a large concentration of vacancies in the *A* sublattice, giving compositions characterized by a $(A'+A''):(B'O_4+B''O_4)$ ratio different from 1:1. The recently reported luminescent properties of $CaLa_{0.6}Eu_{1.4}(MoO_4)_4$, where 25% of the *A* positions are vacant, show an integrated emission intensity of the red light that is similar to that of $CaS: Eu^{2+}$,[11] although this was measured at a single excitation wavelength (465 nm). $CaEu_2(MoO_4)_4$ is described by Qin et al.[2] as one of the three best choices to be used as red-emitting phosphor for WLEDs among the series of $MR_2(MoO_4)_4:Eu^{3+}$ (*M* = Ba, Sr, Ca; *R* = La³⁺, Gd³⁺, Y³⁺). It shows strong excitation at 396 and 465 nm, has a quantum efficiency of 46.7%, a saturated red emission (due to an intensity ratio $(^5D_0 \rightarrow {}^7F_2)/(^5D_0 \rightarrow {}^7F_1)$ of around 11.5), combined with excellent thermal stability. $CaGd_2(MoO_4)_4:Eu^{3+}$ was also investigated, showing an optimal Eu³⁺ concentration at $CaGd_{0.2}Eu_{1.8}(MoO_4)_4$, with properties similar to those of $CaEu_2(MoO_4)_4$.[12] All these compounds were reported to have a disordered scheelite structure with a random distribution of cations and vacancies. However, many scheelite-type oxides have been found recently with complex, incommensurately modulated structures arising from ordering of the *A* cations and vacancies.[14−17]

The incommensurately modulated scheelites known so far exhibit an occupational modulation wave propagating in the *ab* plane of the tetragonal scheelite subcell with a modulation vector $\mathbf{q} = \alpha\mathbf{a}^* + \beta\mathbf{b}^*$.[18] A wide variety of modulation periodicities should be achievable through variation of the chemical composition. This directly affects the placement of the luminescence centers in the structure, and it has been proposed that there is a relation between the incommensurate modulation in the scheelite structure and its luminescent properties.[19] A tentative relation between the quantum yield of the luminescence and a Eu³⁺ association into "dimers" has been postulated.[16] Knowledge of this relation will allow optimizing

the luminescent properties by finding the best spatial arrangement of the rare-earth cations. For instance, the energy transfer between luminescent ions is related to the type of interaction and the distance between the ions. Because of this energy transfer, the probability of nonradiative decay (e.g., at defects) is increased.

A disadvantage of the use of Eu³⁺ in LED conversion phosphors is the limited width of the $^7F_0-{}^5D_2$ absorption band at 465 nm, being considerably narrower than the emission band of the blue LED. Consequently, the overall absorbed fraction of the LED emission is far too low for use in phosphor-converted LEDs. However, in the region of 390−405 nm, there are several possible excitation lines, which can all contribute to the absorption of (near) UV LEDs with emission centered around 395 nm. Katelnikovas et al. showed a significant absorption of the emission of a near-UV LED when using thick $Li_3Ba_2Eu_3(MoO_4)_8$ ceramic disks,[8] combining the increased absorption due to the high dopant concentration and the long optical path length in the ceramic disks. In addition to the applications based on Eu³⁺, the details of the optical properties can be used as a probe for the local symmetry of the dopant ions and thus also of the structure as a whole.[19]

In this paper we demonstrate that the $CaGd_{2(1-x)}Eu_{2x}\square$-$(MoO_4)_{4(1-y)}(WO_4)_{4y}$ ($0 \leq x \leq 1$, $0 \leq y \leq 1$) ($\square$, cation vacancy) scheelite-type solid solutions possess incommensurately modulated crystal structures (including several that were reported before as having a disordered scheelite structure), and we investigate the compositional dependence of the steady state emission and luminescent decay of these compounds by using the Eu³⁺ emission characteristics as a probe of local symmetry.

2. EXPERIMENTAL SECTION

Materials and Sample Preparation. $CaGd_{2(1-x)}Eu_{2x}$-$(MoO_4)_{4(1-y)}(WO_4)_{4y}$ ($0 \leq x \leq 1$, $0 \leq y \leq 1$) solid solutions were synthesized by a solid state reaction from a stoichiometric mixture of $CaEu_2(MoO_4)_4$ and $CaGd_2(MoO_4)_4$, $CaEu_2(WO_4)_4$, and $CaGd_2(WO_4)_4$, respectively. The $CaEu_2(MoO_4)_4$ and $CaGd_2(MoO_4)_4$ were prepared by heating stoichiometric amounts of $CaCO_3$ (99.99%), MoO_3 (99.99%), Eu_2O_3 (99.99%), and Gd_2O_3 (99.99%) at 823 K for 10 h followed by annealing at 1023 K for 96 h in air. The $CaEu_2(WO_4)_4$ and $CaGd_2(WO_4)_4$ were prepared by heating stoichiometric amounts of $CaCO_3$, WO_3 (99.99%), Eu_2O_3, and Gd_2O_3 at 823 K for 10 h followed by annealing at 1203 K for 96 h. Stoichiometric amounts of $CaEu_2(MoO_4)_4$, $CaEu_2(WO_4)_4$, $CaGd_2(MoO_4)_4$, and $CaGd_2(WO_4)_4$ were mixed in proportions corresponding to the required *x* and *y* values in $CaGd_{2(1-x)}Eu_{2x}$-$(MoO_4)_{4(1-y)}(WO_4)_{4y}$ formula and annealed at 1023 K for pure molybdates and at 1203 K for tungsten-containing solid solutions.

Characterization. The cation composition of the $CaR_2(BO_4)_4$ (*R* = Eu, Gd; *B* = Mo, W) compounds was determined by energy-dispersive X-ray spectrometry (EDX) using a Jeol JEM-5510 scanning electron microscope equipped with an EDX spectrometer (Oxford Instruments). EDX analysis was performed at 10 points of each sample. Results of the EDX analysis are summarized in Table S1 of the Supporting Information. The cation ratios found by EDX analysis are close to the intended $CaR_2(BO_4)_4$ compositions.

Powder X-ray diffraction (PXRD) patterns were collected on a Thermo ARL X'TRA powder diffractometer (CuKα radiation, λ = 1.5418 Å, Bragg−Brentano geometry, Peltier-cooled CCD detector). PXRD data were collected at room temperature over the 5°−65° 2θ range with steps of 0.02°. To determine the lattice parameters, Le Bail decomposition[20] was applied using the JANA2006 software.[21]

Samples for transmission electron microscopy were made by crushing the powder in an agate mortar and dispersing it in methanol. After treatment in an ultrasonic bath to disperse the crystallites, a few drops of the solution were placed on a copper grid with a holey carbon

film. Selected area electron diffraction (SAED) and precession electron diffraction (PED) patterns were recorded on a CCD camera with a Philips CM20 transmission electron microscope operating at 200 kV. The PED patterns were generated using a Spinning Star precession attachment. All PED patterns were recorded with a precession angle of 2.5°. The intensities of the recorded reflections were extracted using the in-house developed software IDEA using a pixel summation procedure.[22] The structure refinement was performed using the JANA2006 software.[21] High resolution high angle annular dark field scanning transmission electron microscopy (HAADF-STEM) images were obtained at 300 kV on a FEI Titan 50−80 microscope equipped with a probe aberration corrector. Theoretical HAADF-STEM images were calculated using the STEMsim software.[23]

Luminescence emission and excitation spectra were obtained with a FS920 spectrometer (Edinburgh Instruments), using a 450W xenon light source, double excitation monochromator, and a R928P photomultiplier connected to the emission monochromator. Photoluminescence spectra of all samples were measured under the same conditions. All measurements were performed at room temperature and corrected for the sensitivity of the spectrometer.

3. RESULTS

3.1. Preliminary Characterization.

PXRD patterns of $CaGd_{2(1-x)}Eu_{2x}(MoO_4)_{4(1-y)}(WO_4)_{4y}$ solid solutions revealed a formation of the scheelite-type structure with a body-centered tetragonal scheelite-type subcell (space group $I4_1/a$) in the $0 \leq x \leq 1$, $0 \leq y \leq 0.5$ compositional range and the monoclinically distorted scheelite-type subcell for $0.75 \leq y \leq 1$ (Table S2 of Supporting Information). The onset of the monoclinic distortion is clearly observed in the PXRD patterns of the $y = 0.75$ $CaGd_{0.5}Eu_{1.5}(MoO_4)_{4(1-y)}(WO_4)_{4y}$ compositions (Figure 2) by the increased broadening of the 112/103, 312/303 and 224/107 reflections (Figure 2a, b). At $y = 1$ a pronounced splitting of these reflections becomes evident. Substitution of Gd^{3+} ($r = 1.053$ Å, CN = 8^{24}) by Eu^{3+} ($r = 1.066$ Å, CN = 8^{24}) leads to an increasing unit cell volume, whereas the Mo^{6+}−W^{6+} substitution only weakly influences the lattice parameters because of the similarity of the ionic radii of
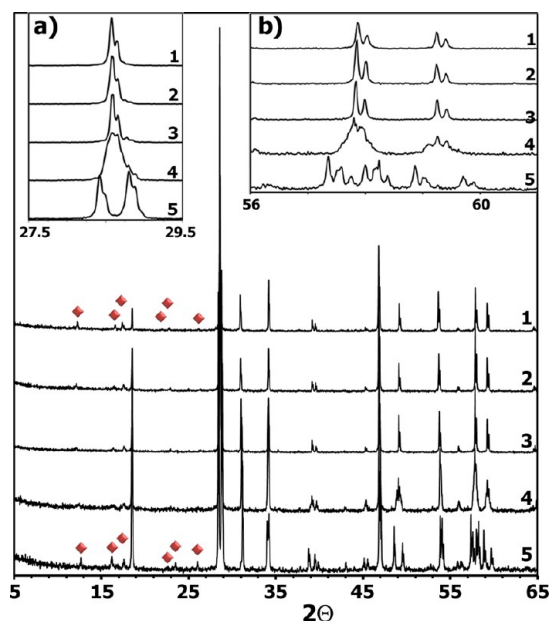
these cations in tetrahedral coordination environment ($r(Mo^{6+})$ = 0.41 Å, $r(W^{6+})$ = 0.42 Å^{24}).

Besides the reflections of the scheelite subcell, weaker reflections are visible in the PXRD patterns (Figure 2) of all $CaGd_{2(1-x)}Eu_{2x}(MoO_4)_{4(1-y)}(WO_4)_{4y}$ solid solutions. Taking into account a well-known tendency of the cation-deficient scheelites to form modulated structures due to cation-vacancy ordering,[14,17,25,26] TEM investigation was undertaken to clarify the nature of these extra reflections.

3.2. Electron Diffraction Study. Representative [001] and [100] ED patterns of $CaEu_2(MoO_4)_4$ and $CaEu_2(WO_4)_4$ are shown in Figure 3. All strong reflections in these patterns

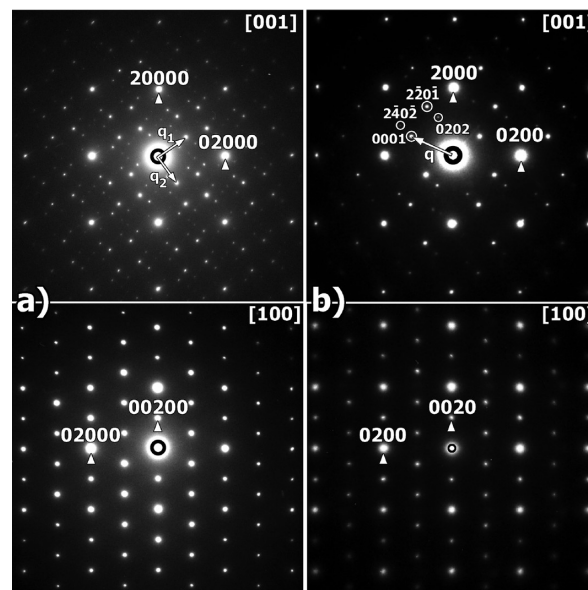**Figure 3.** Comparison between [001] and [100] ED patterns of $CaEu_2(BO_4)_4$ (B = Mo (a), W(b)).

correspond to the scheelite-type subcell with the unit cell parameters determined from PXRD data (Table 2). The [001] ED patterns of $CaEu_2(MoO_4)_4$ (Figure 3a), $CaGd_2(MoO_4)_4$ and all molybdenum-based ($0 \leq y \leq 0.5$ in Table 2) solid solutions are very similar to those reported previously for $Na_{2/7}Gd_{4/7}MoO_4$ with the (3 + 2)-dimensional ((3 + 2)D) incommensurately modulated structure.[17] Indexing of the ED patterns requires five $hklmn$ indexes given by diffraction vector $\mathbf{H} = h\mathbf{a}^* + k\mathbf{b}^* + l\mathbf{c}^* + m\mathbf{q_1} + n\mathbf{q_2}$, with modulation vectors $\mathbf{q_1} \approx 0.54\mathbf{a}^* + 0.82\mathbf{b}^*$ and $\mathbf{q_2} \approx -0.82\mathbf{a}^* + 0.54\mathbf{b}^*$. The reflections with $m,n = 0$ and $m,n \neq 0$ correspond to the main and satellite reflections, respectively (Figure 3 and Figure 4). The $\mathbf{q_1}$ and $\mathbf{q_2}$ vectors are symmetrically dependent according to the tetragonal symmetry of the underlying basic scheelite structure for these compositions. The components of the modulation vectors do not depend significantly on the cation composition: for example, for the $CaGd_{2(1-x)}Eu_{2x}(MoO_4)_4$ series the modulation vectors are $\mathbf{q_1} = 0.542(8)\mathbf{a}^* + 0.818(2)\mathbf{b}^*$ and $\mathbf{q_2} = -0.818(2)\mathbf{a}^* + 0.542(8)\mathbf{b}^*$, as determined from the ED patterns. The $hklmn$: $h + k + l = 2n$ and $hk0mn$: $h, k = 2n$ reflection conditions (Figure 4) are in agreement with the space group $I4_1/a$ for the basic structure. The $00l$: $l \neq 4n$ reflections visible in the [100] ED pattern can be attributed to multiple diffraction. No reflection conditions are imposed on the m and n indexes suggesting the (3 + 2)D superspace group

Figure 2. PXRD patterns of $CaGd_{0.5}Eu_{1.5}(MoO_4)_{4(1-y)}(WO_4)_{4y}$ solid solutions: $y = 0$ (1), 0.25 (2), 0.5 (3), 0.75 (4), 1 (5). Parts of XPRD pattern over the 27.5°−29.5° (a) and 56°−61° 2θ ranges (b) are shown as an inset. Diamonds mark positions of the satellite reflections.
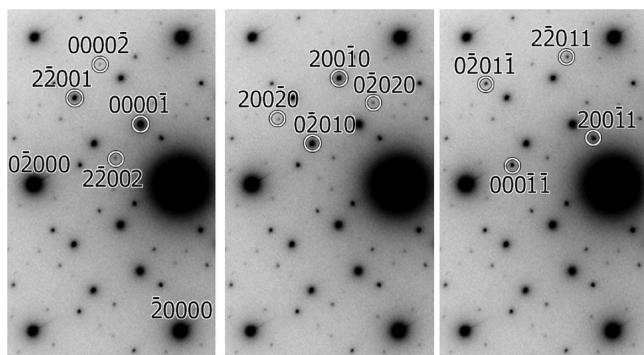
Figure 4. Close-up of the [001] ED pattern of $CaGd_2(MoO_4)_4$ to clarify the indexation. The $hk00n$, $hk0m0$, and $hk0mn$ satellites are marked (from left to right).

$I4_1/a(\alpha,\beta,0)00(-\beta,\alpha,0)00$ (88.2.59.1 in the Stokes−Campbell− van Smaalen notations).[27]

The [001] ED patterns of $CaEu_2(WO_4)_4$ (Figure 3b), $CaGd_2(WO_4)_4$ and all tungsten-based ($0.75 \leq y \leq 1$ in Table 2) solid solutions are very similar to those reported previously for $Ag_{1/8}Pr_{5/8}MoO_4$ with a $(3+1)D$ incommensurately modulated structure[14] and require a single modulation vector with two irrational components to index all satellite reflections. The ED patterns for the $(3+1)D$ modulated $CaGd_{2(1-x)}Eu_{2x}(WO_4)_4$ solid solutions can be described with compositionally independent average modulation vector $\mathbf{q} = 0.58(2) \mathbf{a}^* - 1.221(8)\mathbf{b}^*$. The reflection conditions $hklmn$: $h + k + l = 2n$ and $hk0mn$: $h, k = 2n$ are in agreement with the $(3+1)D$ superspace group $I2/b(\alpha\beta0)00$ (15.1.4.1 in the Stokes−Campbell−van Smaalen notations, $B2/b(\alpha\beta0)00$ in a standard setting).[27]

The modulation vectors measured from the ED patterns were verified by a Le Bail fit of the PXRD pattern of $CaEu_2(MoO_4)_4$ and $CaEu_2(WO_4)_4$. Although only a few satellites were observed on the PXRD patterns, they were sufficient to refine the components of the modulation vectors. The $\mathbf{q}_1 = 0.55255(9)\mathbf{a}^* + 0.8229(1)\mathbf{b}^*$ and $\mathbf{q}_2 = -0.8229(1)\mathbf{a}^* + 0.55255(9)\mathbf{b}^*$ vectors were obtained for $CaEu_2(MoO_4)_4$, whereas for CEW the $\mathbf{q} = 0.5615(3) \mathbf{a}^* - 1.2291(4)\mathbf{b}^*$ vector was refined.

3.3. CaEu₂(WO₄)₄ Structure Solution from Precession Electron Diffraction Data. A crystal structure model for $CaEu_2(WO_4)_4$ was determined and refined using precession electron diffraction (PED) data. Because of the experimental setup in PED, the dynamical effects influencing the relative intensities of the reflections on electron diffraction patterns are drastically suppressed. The measured intensities can therefore be used in structure refinement using a kinematical approximation.[28] Reflections were extracted from 8 different zone axis diffraction patterns. The Friedel pair reflections were averaged and the geometrical correction factor (Lorentz factor) was applied using the formula $C(g,R) = g(1 - (g/2R)^2)^{1/2}$ (g is the reciprocal vector, R is the radius of the Laue circle).[29] The reflection extraction gave 457 reflections in total, of which 51 were $hk01$ satellites, with a resolution up to 0.5 Å. The 8 reflection sets were used in the refinement with individual scale factors to avoid systematic errors introduced by merging the reflections into a single 3D set.

The ordering of Ca, Eu, and vacancies in $CaEu_2(WO_4)_4$ can be modeled using step-like (crenel) occupational modulation functions.[30] According to the chemical composition, the overall

width of the crenel domain for Ca, Eu, and vacancies should be 1/4, 1/2, and 1/4, respectively. Depending on the positioning of the centers of the crenel domains along the a_4 axis, several possible structure models can be defined. The best refinement was achieved using the model where the crenel domain of the vacancies was situated at $x_4^0 = 1/2$ and was surrounded by two crenel domains of Ca ($x_4^0 = 5/16$ and $x_4^0 = 11/16$; $\Delta = 1/8$ each) with the crenel domain of Eu centered at $x_4^0 = 0$ as it is shown in Figure S1 of the Supporting Information. This strongly simplified model implies complete ordering of the Ca and Eu cations in the modulated $CaEu_2(WO_4)_4$ structure. However, such complete ordering would be unlikely taking into account the small charge and size difference between the Eu^{3+} and Ca^{2+} cations ($r(Eu^{3+}) = 1.066$ Å, $r(Ca^{2+}) = 1.12$ Å, CN = 8^{24}). One can assume that this ordering can be smoothed by an extra harmonic occupational modulation imposed over the Ca and Eu crenel domains, as it was implemented earlier in the $KSm(MoO_4)_2$ structure.[26] However, this issue cannot be unambiguously resolved using only the PED data. The limited amount of observed satellites also does not allow taking into account displacive modulations.

A first refinement has been performed with a rigid body approximation for the WO_4 tetrahedra. After convergence was achieved, the rigid body constraints were replaced by soft constraints on W−O distances, and the atomic coordinates of W and O atoms were refined. An attempt was made to refine the overall temperature factor which resulted in a value of $U_{overall} = -0.0073(5)$ Å^2. The slightly negative value of the temperature factor can be attributed to the residual impact of dynamic scattering on the intensities of high angle reflections. The refinement converged with a value $R_{all} = 0.179$ which is good for PED data. The R-value for the main reflections reached $R_{all}(main) = 0.167$, while the value for first order satellite reflections was significantly higher $R_{all}(satellites) = 0.338$. This is most likely because the satellite reflections are much weaker. The relative influence of the dynamical scattering is therefore more significant than for the stronger main reflections. Crystallographic parameters (as measured using information from PXRD data), atomic parameters, and interatomic distances are given in Tables 1, 2, and 3, respectively. The $F_{calculated} - F_{observed}$ plot is shown in Figure S2 of the Supporting Information.

3.4. HAADF-STEM Observations. [001] HAADF-STEM images of $CaEu_2(MoO_4)_4$ and $CaEu_2(WO_4)_4$ are shown in Figure 5. HAADF-STEM images of all $CaGd_{2(1-x)}Eu_{2x}(MoO_4)_4$

Table 1. Selected Crystallographic Data for CaEu₂(WO₄)₄

formula	$CaEu_2(WO_4)_4$
superspace group	$I2/b(\alpha\beta0)00$
a, Å	5.2365(2)
b, Å	5.2629(2)
c, Å	11.4547(4)
γ, deg.	91.152(2)
$\mathbf{q}$	$0.5615(3)\mathbf{a}^* - 1.2291(4)\mathbf{b}^*$
unit cell volume, Å^3	315.62(2)
calculated density, g/cm^3	7.024
Z	1
radiation	electrons, $\lambda = 0.025$ Å
number of reflections	457
θ range, min., max., deg.	0.13, 1.48
number of parameters	17
R_F (all, main refl., first order satellites)	0.179, 0.167, 0.338

Table 2. Atomic Parameters for $CaEu_2(WO_4)_4$

atom	position	x/a	y/b	z/c	x_4^0	Δ
Ca	4e	1/2	1/4	0.8681(17)	5/16	1/8
					11/16	1/8
Eu	4e	1/2	1/4	0.8681(17)	0	1/2
W	4e	1/2	1/4	0.3798(10)		
O1	8f	0.363(3)	0.028(3)	0.284(2)		
O2	8f	0.272(3)	0.365(4)	0.473(2)		

Table 3. Main Interatomic Distances (Å) for $CaEu_2(WO_4)_4$

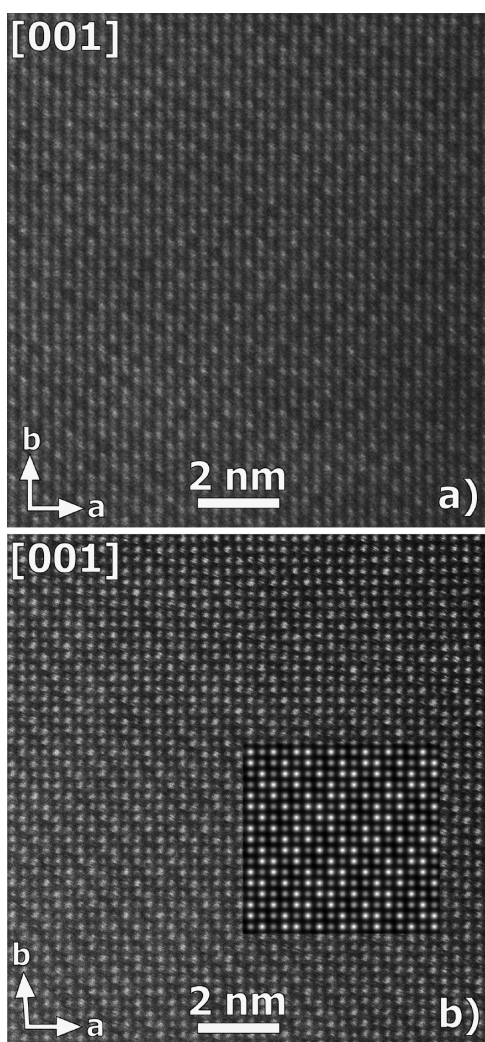|			
Ca–O1 × 2	2.56(2)	Eu–O1 × 2	2.56(2)
Ca–O1 × 2	2.39(3)	Eu–O1 × 2	2.39(3)
Ca–O2 × 2	2.78(2)	Eu–O2 × 2	2.78(2)
Ca–O2 × 2	2.38(3)	Eu–O2 × 2	2.38(3)
W1–O1 × 2	1.75(2)	W1–O2 × 2	1.72(2)

Figure 5. [001] HAADF-STEM images of $CaEu_2(BO_4)_4$ (B = Mo (a), W(b)). The inset in the bottom panel shows the HAADF-STEM image calculated using the refined $CaEu_2(WO_4)_4$ structure for the thickness $t = 20$ nm.

and $CaGd_{2(1-x)}Eu_{2x}(WO_4)_4$ solid solutions do not differ significantly from the images of $CaEu_2(MoO_4)_4$ and $CaEu_2(WO_4)_4$, respectively. On these images the bright dots represent the projected cationic columns. Along the [001] direction, the A and B cations are projected on top of each

other. On the HAADF-STEM images the brightness of the dots is related to the average Z of the atomic column (therefore the oxygen columns are not visible). For the $CaEu_2(MoO_4)_4$ compound, the HAADF-STEM image (Figure 5a) confirms that it is (3 + 2)-dimensionally modulated, and not simply twinned, since the modulation waves propagate along two perpendicular directions in all observed areas and both modulation vectors $\mathbf{q}_1$ and $\mathbf{q}_2$ are clearly present on the Fourier transforms (not shown).

A variation in brightness of the dots on the [001] HAADF-STEM image of $CaEu_2(WO_4)_4$ (Figure 5b) is in agreement with the modulation vector derived from ED patterns. The difference in brightness between the dots is clearly visible resulting in wavy contrast because of the compositional modulation. The simulated [001] HAADF-STEM image of $CaEu_2(WO_4)_4$ was calculated using a $7a \times 9b \times 1c$ commensurate approximant (see inset in Figure 5b). The contrast on the calculated image agrees well with the experimentally observed contrast confirming the correctness of the structure model derived from PED data.

3.5. Luminescent Properties. Figure 6 shows the photoluminescent excitation (PLE) and emission (PL) spectra
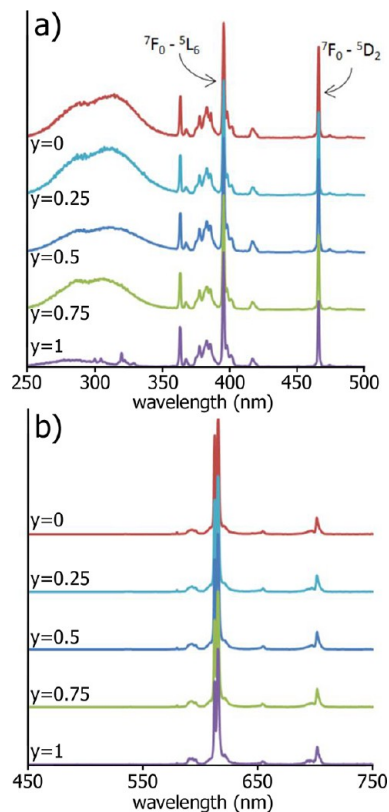

Figure 6. Excitation (λ_{em} = 611 nm) (a) and emission spectrum (λ_{exc} = 300 nm) (b) of $CaGd_{0.5}Eu_{1.5}(MoO_4)_{4(1-y)}(WO_4)_{4y}$ for y = 0; 0.25; 0.5; 0.75; 1.

of $CaGd_{0.5}Eu_{1.5}(MoO_4)_{4(1-y)}(WO_4)_{4y}$ (y = 0, 0.25, 0.5, 0.75, 1). The PLE consists of intraconfigurational $4f^6$-$4f^6$ transitions of Eu^{3+} in the 300 to 500 nm region and a broad band in the region from 250 to 350 nm. The most intense Eu 4f-4f excitations can be attributed to the $^7F_0$–$^5L_6$ (395 nm) and $^7F_0$–$^5D_2$ (465 nm) transitions. The PLE spectra shown in Figure 6 are representative for all $CaGd_{2(1-x)}Eu_{2x}(BO_4)_4$ (B = W, Mo ; x = 0.01, 0.05, 0.10, 0.25, 0.5, 0.75, 1) solid solutions
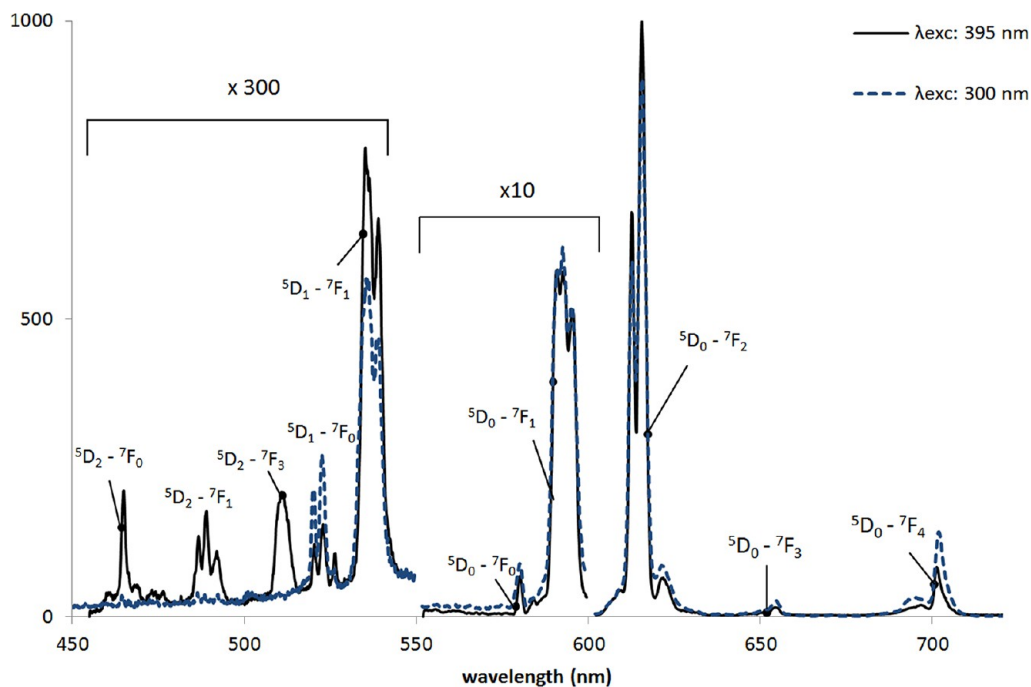

Figure 7. Emission spectra for $CaEu_2(WO_4)_4$ upon excitation into the CT band (300 nm) and the $^5L_6$ level (395 nm) of Eu^{3+}.

as far as the Eu^{3+}-related peaks are concerned, but differ in the broad excitation bands at short wavelength. Moreover, for the CGEW samples three extra Eu^{3+} peaks are observed in the region from 300 to 350 nm.

The PL spectrum of $CaGd_{0.5}Eu_{1.5}(MoO_4)_{4(1-y)}(WO_4)_{4y}$ shows the typical red emission features of Eu^{3+}, including $^5D_0 \rightarrow {}^7F_J$ (J = 0, 1, 2, 3, and 4) (Figure 7) emissions. The most intense peak in the region from 600 to 620 nm is due to the electric dipole transition $^5D_0 \rightarrow {}^7F_2$. The transition at 590 nm is the $^5D_0 \rightarrow {}^7F_1$ magnetic dipole transition.

The dependence of the $^5D_0$ and $^5D_1$ emission on the Eu^{3+} concentration is investigated and illustrated in Figure 8.

The lifetimes of the emission were determined upon excitation at 385 nm with a dye laser (not shown). The $^5D_0$ emission of $CaGd_{0.5}Eu_{1.5}(MoO_4)_4$ exhibits a faster decay (τ =

320 μs) than the tungstate opponent (τ = 400 μs) and for intermediate y values, the decay time gradually increases upon increasing y.

4. DISCUSSION

In contrast to the structures reported in literature for $CaEu_2(MoO_4)_4$, $CaGd_2(MoO_4)_4$, and $CaGd_{2(1-x)}Eu_{2x}(MoO_4)_4$ solid solutions,[12] we demonstrate that these compounds as well as their W-based analogues are not disordered scheelites, but incommensurately modulated structures because of ordering of the A cations and vacancies. $CaGd_{2(1-x)}Eu_{2x}(MoO_4)_{4(1-y)}$-$(WO_4)_{4y}$ solid solutions have either the tetragonal scheelite structure ($0 \leq y \leq 0.5$) which is $(3 + 2)$D modulated or the monoclinically distorted scheelite-type structure ($0.75 \leq y \leq 1$), which is $(3 + 1)$D modulated. The cation and vacancy ordering in $(3 + 1)$D-modulated monoclinic $CaEu_2(WO_4)_4$ structure is demonstrated in Figure 9, showing the $7a \times 9b \times 1c$ commensurate approximant with the $P11a$ symmetry corresponding to a general t-section. The prominent structural motif is formed by columns of the A-site vacancies running along the c axis. The vacant columns are grouped into "dimers" (marked in orange) and "trimers" (marked in yellow) along the [110] direction of the scheelite subcell. This pattern of ordered A cations and vacancies is typical for A-site deficient modulated scheelites and has been observed earlier in the $Na_xEu^{3+}_{(2-x)/3}\square_{(1-2x)/3}MoO_4$ ($0.015 \leq x \leq 1/4$) phases[16] and $Bi_2(MoO_4)_3$.[31] The ordering of cation vacancies in $R_{2/3}\square_{1/3}BO_4$ (R = rare earth elements, B = W, Mo) compounds with the scheelite-type structure depends on the kind of R and B elements in the cation sublattice (Figure 10).[15,31–37] Ordering of cation vacancies along the [110] direction such as in the $CaEu_2(WO_4)_4$ structure was observed before in layers of $R_{2/3}\square_{1/3}BO_4$ compounds with $Eu_2(WO_4)_3$[36] scheelite-type structure (Figure 10a) while vacancies ordered along the [100] direction occurred in the $La_2(MoO_4)_3$ structure (Figure 10b).
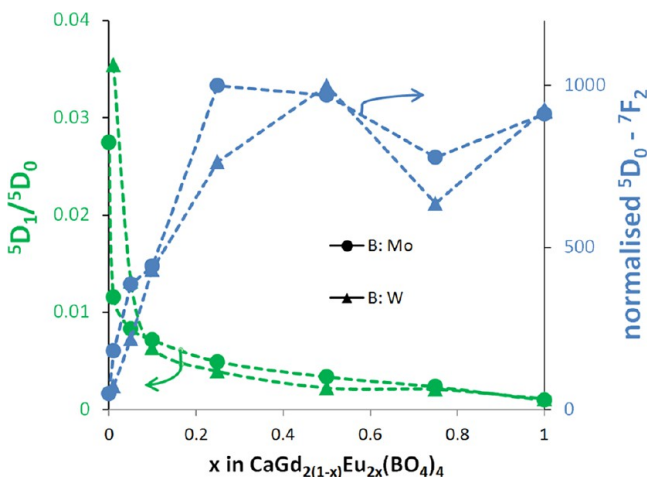
Figure 8. Dependence of the $^5D_0-{}^7F_2$ intensity and the $^5D_1/{}^5D_0$ emission ratio on the Eu concentration in $CaGd_{2(1-x)}Eu_{2x}(BO_4)_4$ after excitation at 300 nm. The circles refer to B = Mo, the triangles to B = W. The connecting lines are a guide to the eye.
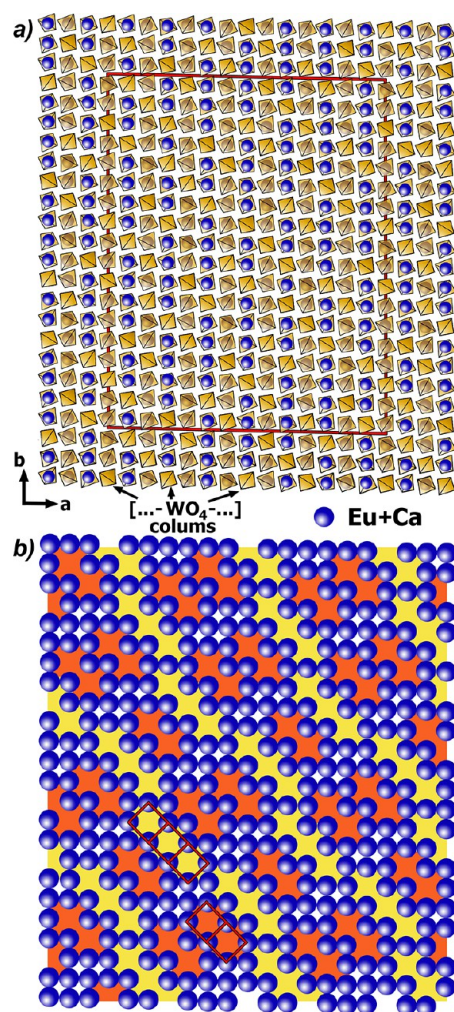
Figure 9. (a) WO_4 tetrahedra, Eu and Ca cations view of the $CaEu_2(WO_4)_4$ structure. Red frame shows $7a \times 9b \times 1c$ commensurate approximant. (b) Outline of cation-vacancy ordering in the $CaEu_2(WO_4)_4$ structure. WO_4 tetrahedra are not shown. The dimers (marked in orange) and trimers (marked in yellow) of the vacant cationic columns are marked with red rectangles.

Figure 10. Layer with AO_8 polyhedra and BO_4 tetrahedra in the scheelite-type structures: $Eu_2(WO_4)_3$ (a) and $La_2(MoO_4)_3$ (b).

The $CaGd_{2(1-x)}Eu_{2x}(MoO_4)_{4(1-y)}(WO_4)_{4y}$ solid solutions demonstrate interesting trends in changing their modulated structures upon the Gd–Eu and Mo–W substitutions. These solid solutions can be considered as a model system where the incommensurate modulation can be monitored as a function of cation size while the amount of the cation vacancies and the average cation charge at the A and B sublattices remain constant upon the isovalent cation replacement. Surprisingly, replacement of the smaller Gd^{3+} ($r = 1.053$ Å, CN = 8[24]) by the larger Eu^{3+} ($r = 1.066$ Å, CN = 8[24]) at the A sublattice does not affect the nature of the incommensurate modulation, although this sublattice is directly affected by the cation-vacancy ordering. In contrast, an increasing replacement of Mo^{6+} by W^{6+} switches the modulation from (3 + 2)D to (3 + 1)D regime. This fact becomes even more astonishing if one takes into account that the Mo^{6+} and W^{6+} cations have almost identical ionic radii ($r(Mo^{6+}) = 0.41$ Å, $r(W^{6+}) = 0.42$ Å[24]). Thus, the charge and/or size difference cannot be a driving force for this switching. One can speculate that the different behavior of the Mo^{6+} and W^{6+} cations could originate from their different electronegativity and, hence, the tendency to
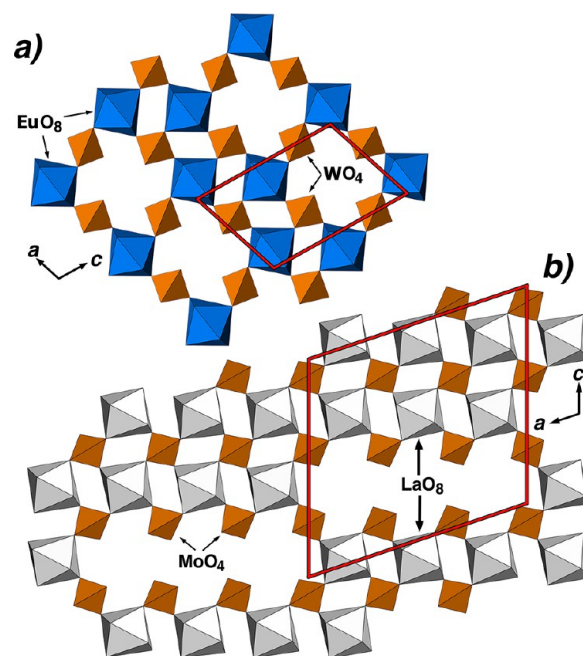
form covalent bonding with oxygen.[38] Increasing covalency of some of the Mo–O and W–O bonds can be a compensating mechanism for the loss of bond valence contribution of the neighboring vacant A site to the bond valence sum of the oxygen atoms. This mechanism can be envisaged as being similar to the second order Jahn–Teller (SOJT) distortion inherent in the octahedrally coordinated Mo^{6+} and W^{6+}. Although the SOJT in the tetrahedrally coordinated Mo^{6+} and W^{6+} generally does not occur because of the much larger HOMO–LUMO energy gap,[39] the situation can be different if the tetrahedron is placed in clearly asymmetric cation environment caused by cation-vacancy ordering followed by underbonding of some oxygen atoms. Verification of this hypothesis needs systematic investigation of the Mo- and W-based modulated scheelites. Synchrotron PXRD experiments on the $CaGd_{2(1-x)}Eu_{2x}(MoO_4)_{4(1-y)}(WO_4)_{4y}$ solid solutions are underway to get the necessary structure information.

Concerning the luminescence spectra, in Figure 6 we can clearly distinguish two broad bands for the $CaGd_{2(1-x)}Eu_{2x}(MoO_4)_4$ samples while we observe only one for the $CaGd_{2(1-x)}Eu_{2x}(WO_4)_4$ samples. For the latter, the broad band centered at 285 nm can presumably be ascribed to a charge transfer (CT) from the 2p orbital of oxygen to the 3d orbital of tungsten inside the WO_4^{2-} group.[40,41] For the $CaGd_{2(1-x)}Eu_{2x}(MoO_4)_4$ samples there is in addition to the O^{2-}–Mo^{6+} CT band (being due to the energy transfer from the oxygen to molybdenum inside the MoO_4^{2-} groups), an extra O^{2-}–Eu^{3+} CT band.[12] This shift in band edge upon increasing molybdenum concentration was also observed by Neeraj et al. for the series $NaGd(WO_4)_{2-x}(MoO_4)_x$:$Eu^{3+}$ and by Cao et al. for the $Ca_{0.54}Sr_{0.22}Eu_{0.08}La_{0.08}\square_{0.08}(MoO_4)_x(WO_4)_{1-x}$ and $Ca_{0.54}Sr_{0.31}Eu_{0.08}Sm_{0.02}\square_{0.05}(MoO_4)_x(WO_4)_{1-x}$ solid solutions.[42–44] In the longer wavelength range we observe the $^7F_0$–$^5L_6$ (395 nm) and $^7F_0$–$^5D_2$ (465 nm) transitions, which match both quite well with the emission spectrum of respectively (near) UV and blue pumping LEDs. However, in the region of 390 to 405 nm several extra peaks are observed, in

contrast to the very sharp peak at 465 nm, resulting in a higher absorption of the LED emission and thus higher conversion efficiency at these wavelengths. This makes the $^7F_0-^5L_6$ transition the preferred pumping wavelength.

For all the samples, the shape of the emission spectrum is almost identical for all europium concentrations. No additional peaks or shifts in peak positions are observed, only the relative intensity changes. Although the emission wavelengths of these 4f-4f transitions are only moderately influenced by the environment of the lanthanide ions, it is possible to make a correlation between the spectrum on the one hand and the symmetry of the site on the other hand. ABO_4 scheelites with the tetragonal symmetry (space group $I4_1/a$) have C_{4h} as 3D point group. The monoclinic distortion of the scheelite-type structure leads to changing the 3D point symmetry from C_{4h} to C_{2h}. As a result, the Ca^{2+} cations, and thus also the Eu^{3+} cations, occupy a site with at most C_2 site symmetry. The lack of inversion symmetry induces the high intensity of the hypersensitive $^5D_0\rightarrow^7F_2$ transition (611 nm). By contrast, the intensity of the $^5D_0-^7F_1$ transition (590 nm) is hardly dependent on the surroundings of the luminescent ion because of its magnetic dipole character. As a consequence, the ratio of both $(^5D_0-^7F_2/^5D_0-^7F_1)$ is often referred to as the asymmetry ratio.[45] For $CaGd_{0.5}Eu_{1.5}(MoO_4)_{4(1-y)}(WO_4)_{4y}$ the values for this ratio vary from 9.93 for $y = 0$ to 7.62 for $y = 1$, which is in line with values reported for other scheelite-based materials.[46] Based on these values, one can expect a higher symmetry (less distortion from inversion symmetry) for the Eu coordination environment in the W-based samples than in the Mo-based samples that contradicts for first glance with the higher crystal symmetry of the Mo-based compounds. However, in the real modulated structure the effective symmetry of the coordination environment depends on the behavior of displacive modulation functions describing the positions of Eu and O atoms.

Another consequence of the C_2 symmetry is the 3-fold splitting of the $^5D_0\rightarrow^7F_1$ and $^5D_1\rightarrow^7F_0$ transitions, which can be observed in Figure 7. The expected 5-fold splitting of the $^5D_0\rightarrow^7F_2$ transition is probably too small to resolve, or involves overlapping peaks. Special attention can be given to the $^5D_0\rightarrow^7F_0$ transition at 580 nm. Since this transition is forbidden, both for electric and magnetic dipole interactions, the intensity can be very low or even non-observable. Yet, for C_2 symmetry the transition is induced, so a peak can be expected at that position. As splitting of the initial and final level, both characterized by $J = 0$, is not possible, observing more than one transition would be an indication of the presence of more than one nonequivalent site for the luminescent Eu^{3+} ions. Since we observe only one peak, the local environment of the Eu^{3+}ions probably remains virtually the same over the whole crystal, remaining 8 oxygen atoms at an average distance of 2.53 Å.[47]

In Figure 8 the dependence of the $^5D_0-^7F_2$ and the $^5D_1/^5D_0$ emission on the concentration of Eu^{3+} in $CaGd_{2(1-x)}Eu_{2x}(BO_4)_4$ (B = Mo, W) is illustrated. As can be seen, the intensity of the $^5D_0-^7F_2$ reaches a maximum for $x = 0.5$. Beyond that, increasing the concentration does not lead to an increase of intensity anymore. This high optimum concentration is not a surprise, as there are many scheelite-based materials for which similar high concentration quenching, or even no concentration quenching at all is reported.[11,48] High concentration quenching might be related to relatively large Eu−Eu distances, which can be estimated as varying in the range of 3.68 to 4.01 Å in the $CaEu_2(WO_4)_4$ structure.

For both the tungstate and the molybdate samples, the ratio of the $^5D_1$ to $^5D_0$ emission is rapidly quenched upon increasing Eu concentration, and this quenching can be explained by the following cross-relaxation process:

$$^5D_{1(ion1)} + {^7F_{0(ion2)}} \rightarrow {^5D_{0(ion1)}} + {^7F_{3(ion2)}}$$
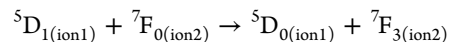
The dependence of the emission on the excitation wavelength is illustrated in Figure 7. Excitation in the CT band (300 nm) does not result in emission from the $^5D_2$ level while emission from this level appears under direct excitation into the $^5L_6$ level. CT excitation apparently skips the $^5D_2$ level during its relaxation process, meaning that the $^5D_1$ and $^5D_0$ energy levels have to be more or less in resonance with the CT minimum.[48]

The recorded lifetimes of the $^5D_0$ emission are in line with previously reported decay times for similar materials.[2,49,50,51] Increasing the Eu concentration leads to a shortening of the decay time for both $y = 1$ and $y = 0$. For $CaEu_2(WO_4)_4$ we obtained a decay time of 284 μs, which is still relatively long given the high europium concentration. For stoichiometric phosphors the nonradiative decay pathways often dominate, resulting in very fast decay times and weak or even absent luminescence.

It can be concluded that the luminescence measurements complement to a large extent the structural data. The detailed analysis of the Eu^{3+} $4f^6$-$4f^6$ multiplets in the emission spectra confirmed that the local oxygen environment of the Eu ions does not vary significantly over the whole modulated structure irrespective of the composition, pointing to the weakness of displacive modulations. Nevertheless, the emission intensity ratio $(^5D_0-^7F_2/^5D_0-F_1)$ revealed a higher effective symmetry of the coordination environment for the tungstate samples compared to the molybdates. The decay measurements showed that concentration quenching occurs for increasing Eu:Gd ratio, but only for high Eu^{3+} concentrations. This could be explained by the relatively large distances between the Eu^{3+} ions in the crystal.

■ ASSOCIATED CONTENT

Ⓢ Supporting Information
EDX analysis results of $CaR_2(BO_4)_4$ (R = Eu, Gd; B = Mo, W) compounds (Table S1). Space symmetry of the basic structure and unit cell parameters for the $CaGd_{2(1-x)}Eu_{2x}(MoO_4)_{4(1-y)}(WO_4)_{4y}$ solid solutions as determined from PXRD patterns (Table S2). Schematic view of the crenel domains in superspace (Figure S1). $F_{calculated} - F_{observed}$ plot for the $CaEu_2(WO_4)_4$ structure refined from PED data (Figure S2). This material is available free of charge via the Internet at http://pubs.acs.org.

■ AUTHOR INFORMATION

Corresponding Author
*E-mail: j.hadermann@ua.ac.be. Phone: +32-32653245. Fax: +32-32653257.

Notes
The authors declare no competing financial interest.

■ REFERENCES

(1) Yen, W. M.; Shionoya, S.; Yamamoto, H. *Phosphor Handbook*, 2nd ed.; CRC Press: Boca Raton, FL, 2007.

(2) Qin, L.; Huang, Y.; Tsuboi, T.; Seo, H. J. *Mater. Res. Bull.* **2012**, *47*, 4498.

(3) Smet, P. F.; Parmentier, A.; Poelman, D. *J. Electrochem. Soc.* **2011**, *158*, R37.

(4) Bachmann, V.; Ronda, C.; Meijerink, A. *Chem. Mater.* **2009**, *21*, 2077.

(5) Li, Y. Q.; Van Steen, J. E. J.; Van Krevel, J. W. H.; Botty, G.; Delsing, A. C. A.; DiSalvo, F. J.; de With, G.; Hintzen, H. T. *J. Alloys Compd.* **2006**, *417*, 273.

(6) Uheda, K.; Hirosaki, N.; Yamamoto, Y.; Naito, A.; Nakajima, T.; Yamamoto, H. *Electrochem. Solid State Lett.* **2006**, *9*, H22.

(7) Li, Y. Q.; Hirosaki, N.; Xie, R. J.; Takeda, T.; Mitomo, M. *Chem. Mater.* **2008**, *20*, 6704.

(8) Poelman, D.; Avci, N.; Smet, P. F. *Opt. Express* **2009**, *17*, 358.

(9) (a) Katelnikovas, A.; Plewa, J.; Sakirzanovas, S.; Dutczak, D.; Enseling, D.; Baur, F.; Winkler, H.; Kareiva, A.; Jüstel, T. *J. Mater. Chem.* **2012**, *22*, 22126. (b) Žukauskas, A.; Vaicekauskas, R.; Ivanauskas, F.; Vaitkevičius, H.; Shur, M. S. *Appl. Phys. Lett.* **2008**, *93*, 051115.

(10) Shao, Q.; Li, H.; Wu, K.; Dong, Y.; Jiang, J. *J. Lumin.* **2009**, *129*, 879.

(11) Haque, M. M.; Kim, D. K. *Mater. Lett.* **2009**, *63*, 793.

(12) Guo, C.; Yang, H. K.; Jeong, J.-H. *J. Lumin.* **2010**, *130*, 1390.

(13) Yi, L.; Zhou, L.; Wang, Z.; Sun, J.; Gong, F.; Wan, W.; Wang, W. *Curr. Appl. Phys.* **2010**, *10*, 208.

(14) Morozov, V. A.; Mironov, A. V.; Lazoryak, B. I.; Khaikina, E. G.; Basovich, O. M.; Rossell, M. D.; Van Tendeloo, G. *J. Solid State Chem.* **2006**, *179*, 1183.

(15) Logvinovich, D.; Arakcheeva, A.; Pattison, P.; Eliseeva, S.; Tome, P.; Marozau, I.; Chapuis, G. *Inorg. Chem.* **2010**, *49*, 1587.

(16) Arakcheeva, A.; Logvinovich, D.; Chapuis, G.; Morozov, V.; Eliseeva, S. V.; Bünzli, J.-C. G.; Pattison, P. *Chem. Sci.* **2012**, *3*, 384.

(17) Morozov, V.; Arakcheeva, A.; Redkin, B.; Sinitsin, V.; Khasanov, S.; M. Raskina, M.; Lebedev, O.; Van Tendeloo, G. *Inorg. Chem.* **2012**, *51*, 5313.

(18) Arakcheeva, A.; Chapuis, G. *Acta Crystallogr., Sect. B* **2008**, *64*, 12.

(19) Tanner, P. A. Lanthanide Luminescence in Solids. In *Lanthanide Luminescence: Photophysical, Analytical and Biological Aspects*; Springer: Berlin, Germany, 2011; p 183.

(20) Le Bail, A.; Duroy, H.; Fourquet, J. L. *Mater. Res. Bull.* **1988**, *23*, 447.

(21) (a) Petrícek, V.; Dusek, M.; Palatinus, L. *JANA2000: the crystallographic computing system*; Institute of Physics: Praha, Czech Republic, 2000. (b) Dusek, M.; Petrícek, V.; Wunschel, M.; Dinnebier, R. E.; Van Smaalen, S. *J. Appl. Crystallogr.* **2001**, *34*, 398.

(22) Van Rompaey, S.; Dachraoui, W.; Turner, S.; Podyacheva, O. Yu.; Tan, H.; Verbeeck, J.; Abakumov, A.; Hadermann, J. *Z. Kristallogr.* **2013**, *228*, 28.

(23) Rosenauer, A.; Schowalter, M. STEMsim-a new software tool for simulation of STEM HAADF Z-contrast imaging. In *Proceedings of the Conference on Microscopy of Semiconducting Materials (15th Cambridge, England, 2007)*; Cullis, A., Midgley, P., Eds.; Springer: Dordrecht, The Netherlands, 2008.

(24) Shannon, R. D. *Acta Crystallogr., Sect. A* **1976**, *32*, 751.

(25) Morozov, V. A.; Arakcheeva, A. V.; Chapuis, G.; Guiblin, N.; Rossell, M. D.; Van Tendeloo, G. *Chem. Mater.* **2006**, *18*, 4075.

(26) Arakcheeva, A.; Pattison, P.; Chapuis, G.; Rossell, M.; Filaretov, A.; Morozov, V.; Van Tendeloo, G. *Acta Crystallogr., Sect. B* **2008**, *64*, 160.

(27) Van Smaalen, S.; Campbell, B. J.; Stokes, H. T. *Acta Crystallogr., Sect. A* **2013**, *69*, 75.

(28) Vincent, R.; Midgley, P. A. *Ultramicroscopy* **1994**, *53*, 271.

(29) Gemmi, M.; Nicolopoulos, S. *Ultramicroscopy* **2007**, *107*, 483−494.

(30) Boucher, F.; Evain, M.; Petricek, V. *Acta Crystallogr., Sect. B* **1996**, *52*, 100.

(31) Van den Elzen, A. F.; Rieck, G. D. *Acta Crystallogr., Sect. B* **1973**, *29*, 2433.

(32) Jeitschko, W. *Acta Crystallogr., Sect. B* **1973**, *29*, 2074.

(33) Gärtner, M.; Abeln, D.; Pring, A.; Wilde, M.; Reller, A. *J. Solid State Chem.* **1994**, *111*, 128.

(34) Wu, M. M.; Peng, J.; Cheng, Y. Z.; Wang, H.; Yu, Z. X.; Chen, D. F.; Hu, Z. B. *Solid State Sci.* **2006**, *8*, 665.

(35) Wang, S.-F.; Rao, K. K.; Wang, Y.-R.; Hsu, Y.-F.; Chen, S.-H.; Lu, Y.-C. *J. Am. Ceram. Soc.* **2009**, *92*, 1732.

(36) Boulahaya, K.; Parras, M.; Gonzalez-Calbet, J. M. *Eur. J. Inorg. Chem.* **2005**, *5*, 967−970.

(37) Templeton, H. D.; Zalkin, A. *Acta Crystallogr., Sect. B* **1963**, *16*, 762.

(38) Eng, H. W.; Barnes, P. W.; Auer, B. M.; Woodward, P. M. *J. Solid State Chem.* **2003**, *175*, 94.

(39) Woodward, P. M. Mizoguchi, H.; Kim, Y.-I.; Stoltzfus, M. W. The Electronic Structure of Metal Oxides. In *Metal Oxides, Chemistry and Applications*; Taylor & Francis: Boca Raton, FL, 2006; pp 133−194.

(40) Shi, S.; Liu, X.; Gao, J.; Zhou, J. *Spectrochim. Acta, Part A* **2008**, *69*, 396.

(41) Blasse, G. The luminescence of Closed-shell transition-metal complexes. New developments. In *Structure and bonding*; Springer Verlag: New York1980; pp 1−41.

(42) Neeraj, S.; Kijima, N.; Cheetham, A. K. *Chem. Phys. Lett.* **2004**, *387*, 2.

(43) Cao, F.-b.; Tian, Y.-w.; Chen, Y.-j.; Xia, L.-j.; Wu. *J. Lumin.* **2009**, *129*, 585.

(44) Cao, F.-b.; Tian, Y.-w.; Chen, Y.-j.; Xia, L.-j.; Wu, Q. *J. Alloys Compd.* **2009**, *475*, 387.

(45) Werts, M. H. V.; Jukes, R. T. F.; Verhoeven, J. W. *Phys. Chem. Chem. Phys.* **2002**, *4*, 1542.

(46) Su, Y.; Li, L.; Li, G. *Chem. Mater.* **2008**, *20*, 6060.

(47) Blasse, G.; Bril, A.; Nieuwpoort, W. C. *J. Phys. Chem. Solids* **1966**, *27*, 1587.

(48) Li, H.; Yang, H. K.; Moon, B. K.; Choi, B. C.; Jeong, J. H.; Jang, K.; Lee, H. S.; Yi, S. S. *J. Electrochem. Soc.* **2012**, *159*, J61.

(49) Struck, C. W.; Fonger, W. H. *J. Lumin.* **1970**, *1* (2), 456−469.

(50) Wu, H.; Hu, Y.; Zhang, W.; Kang, F.; Li, N.; Ju, G. *J. Sol.-Gel. Sci. Technol.* **2012**, *62*, 227.

(51) Cao, F. B.; Li, L. S.; Tian, Y. W.; Chen, Y. J.; Wu, X. R. *Thin Solid Films* **2011**, *519*, 7971.